Rhodium-Based Metal-Organic Polyhedra Assemblies for Selective CO2 Photoreduction

A. Ghosh, A. Legrand, R. Rajapaksha, G. Craig, C. Sassoye, G. Balazs, D. Farrusseng, S. Furukawa, J. Canivet, F. Wisser

Rhodium-based metal-organic polyhedra assemblies for selective CO_2 photoreduction.

Ashta C. Ghosh,[†,Δ] Alexandre Legrand,[#,Δ] Rémy Rajapaksha,[†] Gavin A. Craig,[#,♦] Capucine Sassoye,[□] Gabor Balazs,[‡] David Farrusseng,[†] Shuhei Furukawa,[#,*] Jérôme Canivet,[†,*] Florian M. Wisser[‡,*]

[†] Université de Lyon, Université Claude Bernard Lyon 1, CNRS, IRCELYON - UMR 5256, 2 Avenue Albert Einstein, 69626 Villeurbanne Cedex, France.

[#] Institute for Integrated Cell-Material Sciences (WPI-iCeMS), Kyoto University, Yoshida, Sakyo-ku, Kyoto 606-8501, Japan.

[□] Sorbonne Université, Chimie de la Matière Condensée de Paris - UMR 7574, 4 Place Jussieu, 75005 PARIS, France

[‡] Institute of Inorganic Chemistry, University of Regensburg, 93040 Regensburg, Germany.

KEYWORDS. CO_2 reduction, dirhodium paddlewheels, formic acid, heterogeneous photocatalysis, metal-organic polyhedra

ABSTRACT: Heterogenization of molecular catalysts via their immobilization within extended structures often results in a lowering of their catalytic properties due to a change in their coordination sphere. Metal-organic polyhedra (MOPs) are an emerging class of well-defined hybrid compounds with a high number of accessible metal sites organised around an inner cavity, making them appealing candidates for catalytic applications. Here we demonstrate a design strategy that enhances the catalytic properties of dirhodium paddlewheels heterogenized within a MOP (Rh-MOP) and its three-dimensional assembled supramolecular structures, which proved to be very efficient catalysts for the selective photochemical reduction of carbon dioxide to formic acid. Surprisingly, the catalytic activity per Rh atom is higher in the supramolecular structures than in its molecular sub-unit Rh-MOP or in Rh-MOF, and yields turnover frequencies of up to 60 h^{-1} and production rates of approx. 76 mmole formic acid per gram of catalyst per hour, unprecedented in heterogeneous photocatalysis, demonstrating the high potential of MOPs as catalysts for the photoreduction of CO_2. This opens new perspectives for the electronic design of discrete molecular architectures with accessible metal sites for the production of solar fuels. The enhanced catalytic activity is investigated by XPS spectroscopy and electrochemical characterization, showing that self-assembly into supramolecular polymers increases the electron density on the active site, making the overall reaction thermodynamically more favourable. The catalyst can be recycled without loss of activity and with no change of its molecular structure as shown by pair distribution function analysis.

INTRODUCTION

A fruitful strategy in the design of molecularly-defined heterogeneous catalysts is the immobilization of isolated active sites within a host framework whose intrinsic porosity ensures the accessibility of the active site. Importantly and beyond technical advantages like direct catalyst separation from product, heterogenization can also stabilize accessible metal sites that act as single atom catalysts, avoiding the formation of metal clusters and maintaining a high concentration of active sites.[1–6]

Thus, the controlled structuration of accessible metal sites as a key catalytic component in a porous framework would confer appealing catalytic properties combining high site density and stabilization with active site accessibility on the corresponding materials. However, the integration of catalytically active centres into a solid support often results in an intrinsic reduction of their activity compared to their homogeneous molecular counterparts.[3,7,8] The reasons for this decrease in catalytic activity are not yet fully understood. Recently we demonstrated that one crucial factor resulting in a lower catalytic activity after heterogenization is the change in the electron density on the catalytically active site caused by the heterogenization itself.[9]

In the context of catalytically active accessible metal sites, $Rh_2^{II,II}$ paddlewheel complexes, in which the removal of labile ligands from the axial position of the paddlewheel can give access to open Rh metal sites, stand out by their high chemical stability as well as their variety of accessible redox states, including $Rh_2^{II,I}$ and $Rh_2^{II,III}$ oxidation states.[10,11] Consequently, $Rh_2^{II,II}$ paddlewheel complexes have attracted interest in a large range of catalytic reactions,[11] including cyclopropanation,[12,13] hydrogenation,[14–17] ethylene dimerization,[18] or photocatalytic hydrogen evolution reaction.[10,19,20] So far, the heterogenization of the $Rh_2^{II,II}$ paddlewheel as a catalytic centre has been limited to their immobilization within supramolecular structures (through non-covalent interaction) or coordination polymers and metal-organic frame-

works (MOFs). A controlled arrangement of $Rh_2^{II,II}$ paddlewheels has recently been reported in metal-organic cages, also called metal-organic polyhedra (MOPs), which are discrete molecular structures, self-assembled from bent ligands and metal precursors. [21–23] As one of the smallest porous units, MOPs have been used as templates to accommodate and control properties of various guests, and have shown promising applications in, sorption, separation, and sensing.[21,24–27] In catalytic applications MOPs have been used mostly as nanocontainers, encapsulating catalytically active species,[28] or as nanoreactors, with grafted organocatalysts or inorganic complexes to their linker backbone.[29–32] So far, the use of the secondary building unit of metal-organic polyhedra as a catalytic centre is still scarce,[33–35] and their potential as a photocatalyst is as yet unexplored.

Here, we explore the catalytic activity of the preformed MOP $[Rh_2(bdc)_2]_{12}$ (bdc = benzene-1,3-dicarboxylate) and their assembled supramolecular structures formed by coordination with 1,4-bis(imidazol-1-ylmethyl)benzene as ditopic N-donor linkers. Depending on the amount of N-donor linker, the materials are obtained as colloidal particles (Rh-CPP) or aerogels (Rh-SAG, Figure 1).[36] As heterogeneous catalysts in the photocatalytic reduction of CO_2 to formic acid, they yield unexpectedly high catalytic activities, outperforming both molecular $Rh_2^{II,II}$ paddlewheel complexes and other heterogeneous photocatalysts. We use pair distribution function analysis, XPS, *in situ* EPR spectroscopy and electrochemical measurements to rationalize these findings. The key favourable properties of these catalysts are their high density of Rh active sites, their high accessibility due to the cage structure of the MOP, and the increased electron density of the active site induced by immobilization in a supramolecular polymer with a suitable electron donating linker.

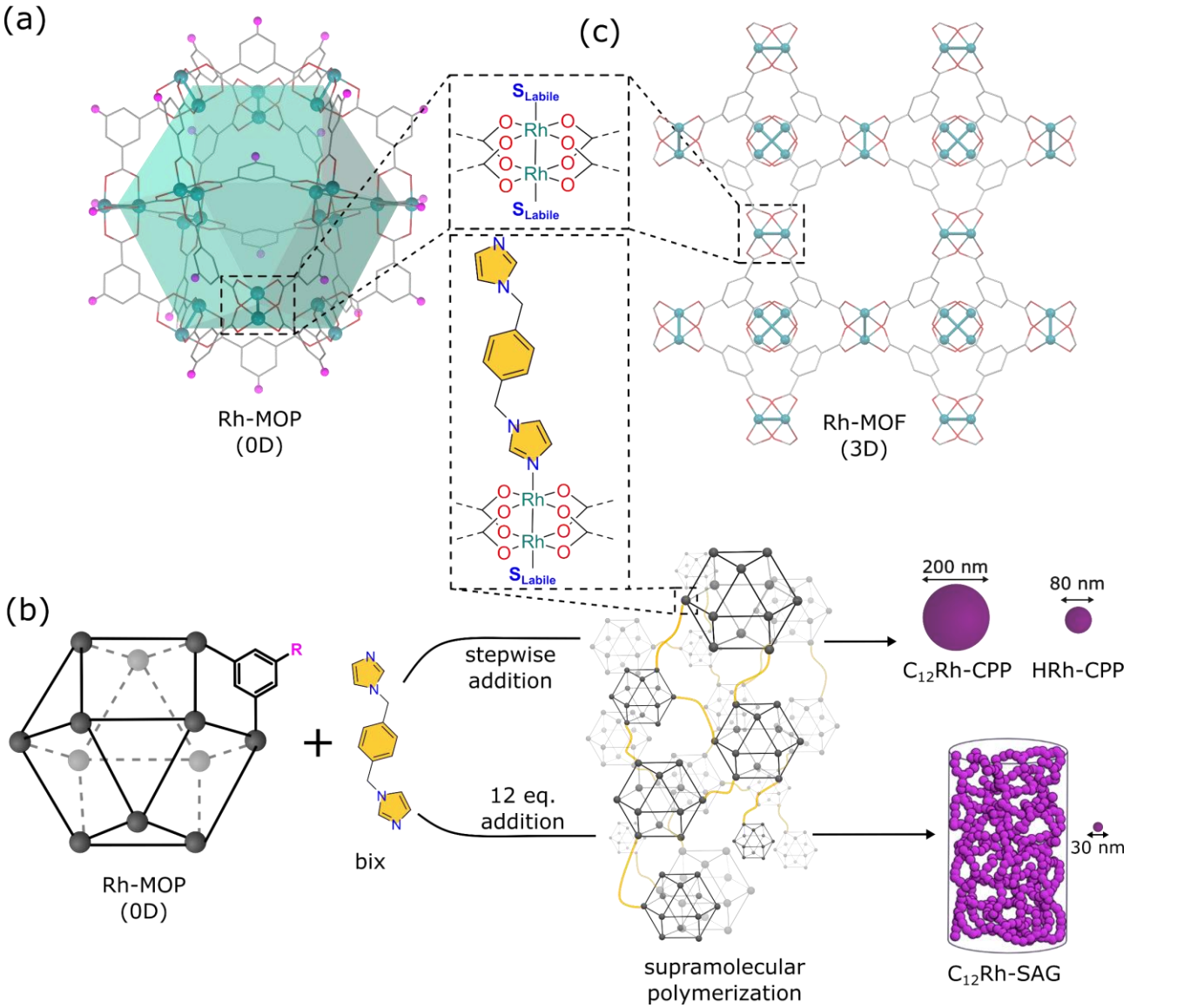

Figure 1. Schematic representation of (a) the Rh-MOP, $[Rh_2(R\text{-}bdc)_2]_{12}$ (R = 5-dodecoxy (C_{12}) or H), with the green polygon highlighting the cuboctahedral geometry of the cage and the purple atoms the substituent groups in the five positions of the isophthalic acid (R-bdc). The structure is calculated from the single crystal data of $[Rh_2(H\text{-}bdc)_2]_{12}$.[37] (b) Schematic representation of the supramolecular polymerization reaction between Rh-MOP and bix, which leads to the formation of colloidal parti-

cles (Rh-CPP) when bix is added stepwise or to the formation of a colloidal gel network when 12 eq. of bix are added. The gel is then transformed into the corresponding colloidal aerogel (Rh-SAG) after solvent exchange and $ScCO_2$ drying process. (c) Schematic representation of the Rh-MOF, $[Rh_3BTC_2]_n$, derived from isostructural Cu_3BTC_2 (because of the absence of experimental $[Rh_3BTC_2]_n$ structure) view along the crystallographic a axis (CCDC 827934). H-atoms are omitted for clarity. Color code: Rh green, O red and C grey. The Rh-MOP and Rh-MOF possess two axial, accessible metal sites in the rhodium paddlewheel, while for the assembled colloidal particles and aerogel based on Rh-MOP building blocks, the metal nodes are partially coordinated by bix molecules in the exohedral axial site (at the MOP surface).

RESULTS AND DISCUSSION

Design of $Rh_2^{II,II}$ paddlewheel photocatalysts. Previously, we reported the self-assembly of isophthalic acid derivatives with rhodium paddlewheel precursors ($Rh_2(OAc)_4$) to form stable rhodium-based cuboctahedral MOPs, which possess an internal cavity with a diameter of ~ 1.2 nm and window openings of 0.4 and 0.7 nm for trigonal and square shaped apertures respectively, as determined using an automated structural analysis of molecular pores.[38] In case of isophthalic acid (H-bdc) as ligand the MOP $[Rh_2(H\text{-}bdc)_2]_{12}$ is obtained,[37] and in case of 5-dodecoxybenzene-1,3-dicarboxylic acid (C_{12}-bdc) the MOP $[Rh_2(C_{12}\text{-}bdc)_2]_{12}$,[39] called hereafter **HRh-MOP** and **C_{12}Rh-MOP** respectively (**Erreur ! Source du renvoi introuvable.**a). In the case of **HRh-MOP**, it is necessary to solubilize the cage through the coordination of 1-dodecyl-1H-imidazole (diz), to the exohedral axial metal sites of the MOP, prior to any supramolecular polymerization reaction. Further reaction of the exohedral Rh(II) ions of the Rh-MOPs with 1,4-bis(imidazol-1-ylmethyl)benzene (bix) as a ditopic N-donor ligand drives their self-assembly into supramolecular polymers (

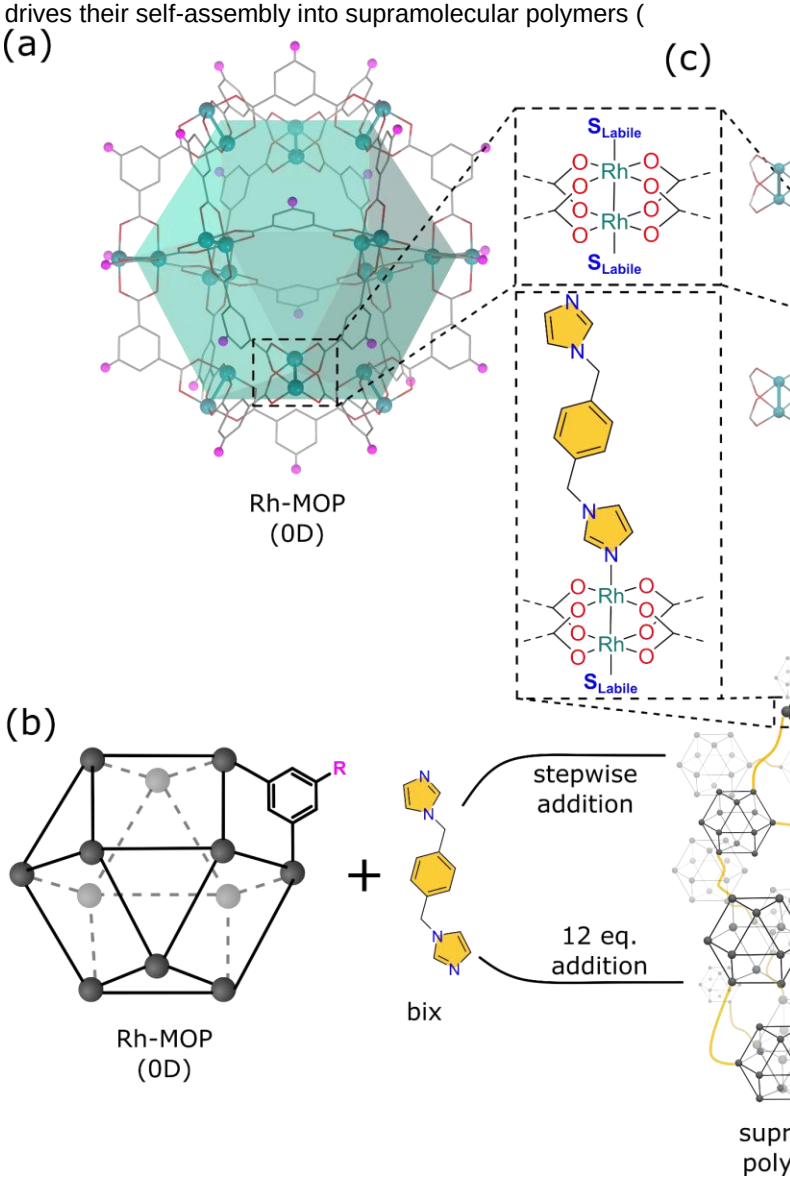

Figure 1b).[36] During the stepwise addition of bix (see SI section S2 for details), the supramolecular polymers can be obtained as spherical coordination polymer particles (CPP) with an average diameter of 206 ± 63 nm and 79 ± 18 nm for **C_{12}Rh-CPP** and **HRh-CPP** respectively (Figure S5a, b). When adding the Rh-MOP to 12 molar equivalents of bix, a colloidal gel network, made of particles of 30 nm, is formed. Further processing of the gel with supercritical CO_2 dryer lead to the formation of a supramolecular aerogel after solvent removal (**C_{12}Rh-SAG**, Figure S8).[36] The **C_{12}Rh-CPP** has an average composition of $[Rh_2(C_{12}\text{-}bdc)_2]_{12}(bix)_{5.1}$ (Figure S6a), while the content of bix linker is approximately double in the aerogel, giving a composition of $[Rh_2(C_{12}$-

bdc)$_2$]$_{12}$(bix)$_{9.8}$ (Figure S9).[36] For **HRh-CPP**, the composition is [Rh$_2$(H-bdc)$_2$]$_{12}$(bix)$_{8.2}$(diz)$_{3.3}$ (Figure S6b). All supramolecular polymers are built from well-defined building-blocks but lack long range order.

In the Rh-CPP and Rh-SAG materials, the endohedral axial rhodium atom of each Rh paddlewheel is an accessible metal site pointing towards the inside of the porous cage, while the exohedral one can be coordinated by bix molecules. For comparison, we also synthesized a Rh-paddlewheel-containing Rh-MOF, [Rh$_3$(BTC)$_2$]$_n$,[40] which was obtained by reacting Rh$_2$(OAc)$_4$ with benzene-1,3,5-tricarboxylic acid (H$_3$BTC) in aqueous acetic acid at 150 °C. In this material, the Rh$_2$ paddlewheels are linked in all three dimensions by bridging BTC^{3-} molecules, resulting in a rigid, crystalline, porous framework (

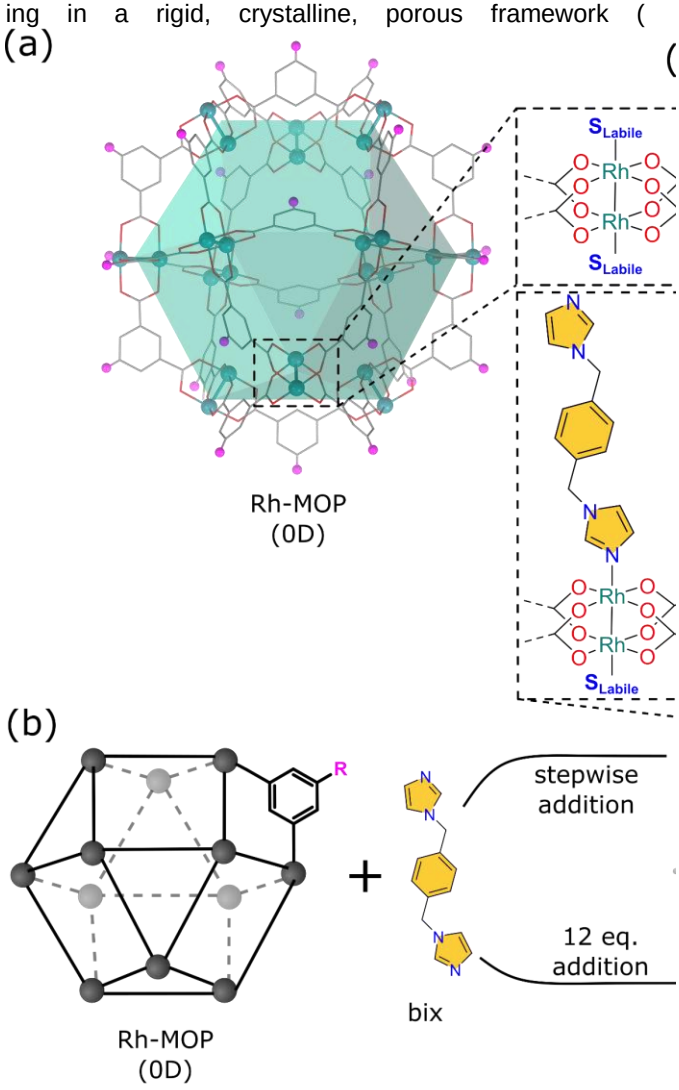

Figure 1c), its properties in line with results from literature (SI section S2, Figure S13 for further characterization).[40] In a similar fashion to the Rh-MOPs, the Rh-MOF contains Rh paddlewheels with accessible metal sites in the axial positions, but with smaller estimated pore sizes of 0.8 compared to 1.2 nm for Rh-MOP. With the exception of **C$_{12}$Rh-MOP**, all of the materials are porous towards nitrogen at 77 K, with sharp uptakes at low pressures characteristic of microporous materials, and apparent surface areas of 20 m^2/g, 100 m^2/g, 160 m^2/g and 880 m^2/g for **C$_{12}$Rh-CPP**, **HRh-CPP**, **C$_{12}$Rh-SAG** and **HRh-MOP** respectively (Figure S10), and 870 m^2/g for Rh-MOF (Figure S13a). The pore size distribution (PSD) demonstrates that all of the samples have pores in the microporous range, in good agreement with the dimensions of the cuboctahedral cage (Figure S11). In addition, the supramolecular systems present extrinsic porosity arising from the free volume between the MOPs within the colloidal particles. The smaller surface areas observed for the C$_{12}$Rh-systems compared to HRh-systems as well as Rh-MOF are explained by the bulky alkyl chain hindering the access to the MOP cavity and occupying free volume in the materials. It is worth noting that Rh-MOF, Rh-MOPs and the supramolecular polymers **C$_{12}$Rh-CPP**, **C$_{12}$Rh-SAG** and **HRh-CPP** are accessible for CO$_2$.[36,40,41]

Photocatalytic CO$_2$ reduction. In the context of greenhouse gases reduction and solar fuel production, Rh paddlewheel-based materials have never been reported as CO$_2$ reduction catalysts so far. Thus, we evaluated the performance of the **Rh-MOPs**, as well as that of solid **Rh-CPP**s and **Rh-SAG**, as catalysts in the photochemical CO$_2$ reduction in the presence of Ru(bpy)$_3$Cl$_2$ as photosensitizer and triethanolamine (TEOA) as sacrificial electron donor. For the sake of comparison, the catalytic behaviour of Rh-paddlewheels has also been studied in molecular Rh$_2$(OAc)$_4$ and when used as building block for the construction of Rh-MOF material.

The photocatalytic CO$_2$ reduction experiments were carried out in a mixture of acetonitrile as solvent and triethanolamine as proton and electron donor and using a solar simulator as light source. All materials showed catalytic activity for the transformation of CO$_2$ into formic acid as the only carbon containing product (Figure 2a, *vide infra*). To calculate the catalytic activity, we considered that – consistent with reports from hydrogen evolution reaction[10,11,20] and electrochemical CO$_2$ reduction[11] – the catalytically active site consists of one Rh$_2$ paddlewheel unit, independently of whether there are one or two accessible metal sites per paddlewheel. The lowest catalytic activity was obtained with the Rh-MOF, with a turnover frequency (*TOF*) of only 5 h^{-1} and a production rate *R* of up to 10.1 mmol$_{formic\ acid}$/g$_{cat}$/h (Figure 2a, Table S6, & Table S7). In a clear contrast, the supramolecular polymers, Rh-CPPs and Rh-SAG, achieved *TOF*s of up to 59 h^{-1} (Figure 2a, *R* = 76 mmol$_{formic\ acid}$/g$_{cat}$/h, Table S6), independently of their apparent surface area. Gas phase analysis of the reaction head space as well as carbon-13 labelling experiments using ^{13}CO$_2$, confirmed that formic acid is the only carbon containing reduction product and it was produced exclusively from CO$_2$, implying that the network had not decomposed (SI, section 6.3, Figures S26, S27).

Rationalization of catalytic activities. Despite their different morphology and porosity, **C$_{12}$Rh-CPP** and **C$_{12}$Rh-SAG** show slightly higher catalytic activities than their molecular building block **C$_{12}$Rh-MOP** (*TOF* = 52 h^{-1}). The main structural difference between the isolated **C$_{12}$Rh-MOP** and the 3D materials **C$_{12}$Rh-CPP** and

C_{12}Rh-SAG results from the coordination of the bix ligands to the exohedral axial positions of the **C_{12}Rh-MOP** thus (i) introducing extrinsic porosity to the materials and (ii) changing the molecular environment of the active site (

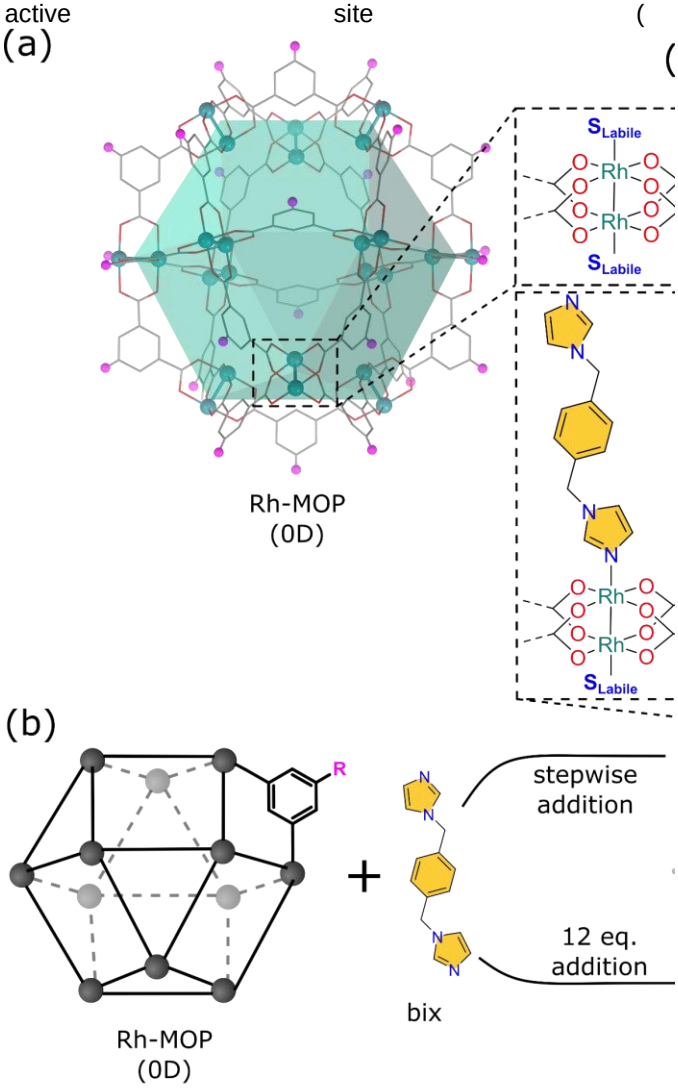

Figure 1). In order to mimic the coordination by bix N-atoms in **C_{12}Rh-CPP** and **C_{12}Rh-SAG** solids, the exohedral Rh atoms of the pristine **C_{12}Rh-MOP** were capped by reaction with 12 equivalents of monodentate 1-benzylimidazole (bnix) to yield $[Rh_2(C_{12}\text{-bdc})_2]_{12}(bnix)_{12}$ (**C_{12}Rh-MOP$_{bnix}$**) as a molecular model of the corresponding CPP and SAG (Figure S2). **C_{12}Rh-MOP$_{bnix}$** gave rise to an increased catalytic activity (*TOF* = 58 h^{-1}), very similar to the activity observed for **C_{12}Rh-CPP** and **C_{12}Rh-SAG**. We thus infer from this trend that (i) the reaction is not limited to surface processes in the heterogeneous supramolecular polymers and (ii) the inner part of the heterogeneous catalysts is indeed accessible for the reactants, including TEOA. Importantly, the coordination of monotopic bnix molecules to the exohedral Rh atoms of the Rh_2 paddlewheel slightly increases the electron density on Rh centres, resulting in higher catalytic activity (*vide infra*). It is worth noticing that the substituents of the bdc linker in the 5-position of the Rh-MOP have an effect on the catalytic activity. Indeed, when the alkoxy group of the **C_{12}Rh-MOP** is replaced by hydrogen (**HRh-MOP**), the *TOF* and production rate show a slight decrease (*TOF* = 43 h^{-1} vs. 52 h^{-1} for **C_{12}Rh-MOP**). As for **C_{12}Rh-MOP**, heterogenization of **HRh-MOP** in the corresponding **HRh-CPP** material results in an increase of *TOF* to approx. 56 h^{-1} (Table S6, entry 26). The slightly higher catalytic activities of the **C_{12}Rh-MOP** based materials can be explained by an higher electron density on the active Rh site in those materials, caused by the higher electron donating properties of the alkyl chain when compared to the hydrogen atom in the 5-position of the isophthalate linkers.[9,42]

Despite having structurally similar Rh-paddlewheel building units, the Rh-MOP molecular systems show a two-fold increase in TOF compared to the $Rh_2(OAc)_4$ (Table S4, entries 1, 2 & 30). Here we note that during photocatalysis $Rh_2(OAc)_4$ decomposes into Rh nanoparticles, as evidenced by TEM analysis of the reaction mixture (see Figure S24). On the other hand, we did not observe any indication of decomposition in the Rh-MOP molecular systems, e.g. leaching of paramagnetic Rh species or formation of Rh nanoparticles. Thus, the increase in turnover numbers is most likely caused by a stabilisation of the dirhodium moiety within the Rh-MOPs. Similarly, for the extended structures, the Rh-MOP-based catalysts show a twelve-fold increase in TOF compared to the Rh-MOF. To understand these differences in catalytic activity, X-ray photoelectron spectroscopy (XPS) is an asset to investigate changes in electron density on the active site. Indeed, the catalytic activity in heterogeneous molecular photocatalysis in a series of structurally comparable heterogenized catalysts has recently been demonstrated to depend on the electron density of the active site. We recently reported that for Rh catalysed CO_2 reduction reaction, a decrease in rhodium electron binding energy (*EBE*), corresponding to a higher electron density on the rhodium, results in a higher catalytic activity.[9] Here we observed similar behaviour. Rh atoms in the Rh-MOF show a significant higher electron binding energy (309.6 eV) compared to the Rh atoms in the Rh-MOP (309.3 eV) or the Rh-CPP and Rh-SAG (309.2 eV, Figure 2b, c & Figure S14).

Thus, the lower catalytic activity of the Rh-MOF can be attributed to the lower electron density on the active site (higher *EBE*), directly affecting the reaction rate. This difference in *EBE* is directly related to replacing the electron donating substituents in the 5 position of the benzene moiety in Rh-MOPs by an electron withdrawing Rh-carboxylate. This is further reflected by an increase in the substituents' Hammett constant, an empirical descriptor of the electron density, for the more electron withdrawing group.[5,9,42,43]

The Rh-MOP based polymers outperform the most active heterogeneous photocatalyst for the selective transformation of carbon dioxide into formic acid reported so far by at least one order of magnitude when comparing production rates to the catalysts based on different metal catechols and metal-oxo clusters, as well as Cu, Mn, Rh or Ru-polypyridyl complexes independently of the nature of the host (MOFs, porous organic polymers, graphitic carbon nitride, semiconductor, Table S9).[9,44–50] For those

catalysts, production rates of up to 4 $mmol_{formic\ acid}/g_{cat}/h$ were reported (Table S9), while **HRh-CPP** reaches 76 $mmol_{formic\ acid}/g_{cat}/h$.

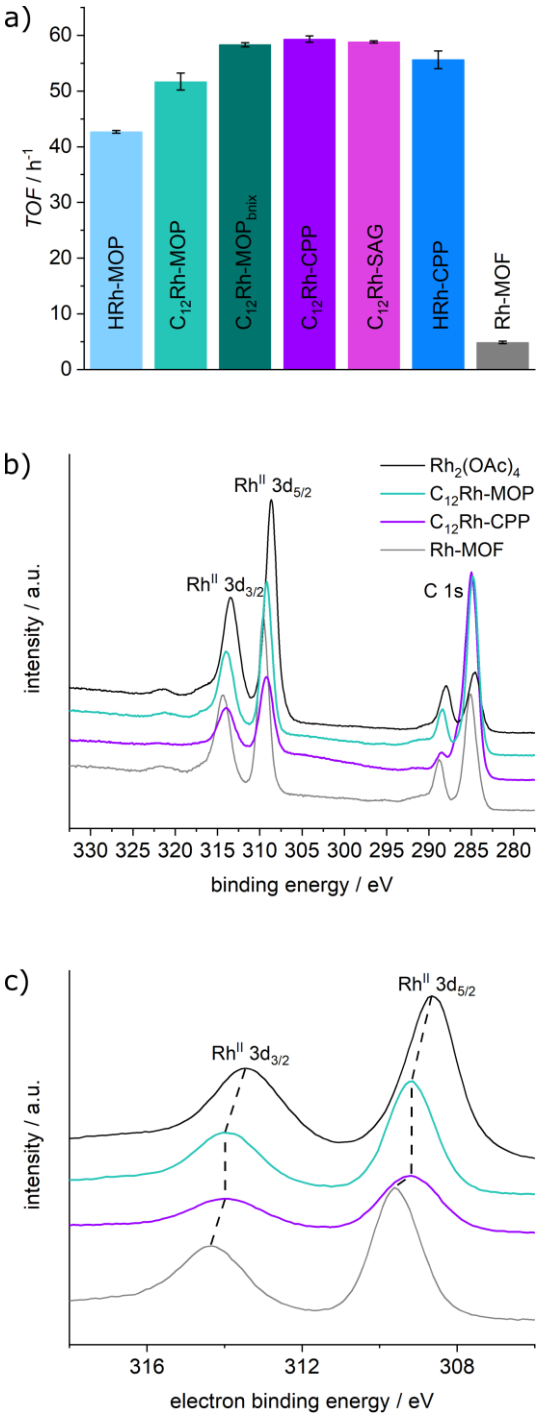

Figure 2. a) Overview of catalytic activity in photocatalytic CO_2 reduction over various Rh_2-based catalysts in the presence of $Ru(bpy)_3Cl_2$ as photosensitizer. Reaction conditions: 0.05 mM catalyst, 1 mM $Ru(bpy)_3Cl_2$ in ACN : TEOA (5 : 1, V : V), 2 h, ABA class solar simulator without filter. b) XPS spectra of Rh_3BTC_2, $Rh_2(OAc)_4$, **C_{12}Rh-MOP** and **C_{12}Rh-CPP** showing C 1s and Rh 3d binding energy region and c) enlarged region of Rh 3d binding energy. Change in the electron binding energy is highlighted by the dotted line. Deconvoluted spectra are provided in Figure S14.

Here we note that lower catalytic activities were observed for the MOP-based catalysts when the solar simulator was replaced by a 200 W Hg lamp as light source (Table S8), similar to the setup used in literature.[9,44–47] However, they still outperform the best heterogeneous catalysts, a porous polymer embedding a Cp*Rh(bpy) molecular complex (Cp*Rh@BpyMP-1), reported so far for the CO_2-to-formate photoreduction,[9] by one order of magnitude, even when studied under identical conditions (Tables S7 – S9).

Thermodynamic driving force. The huge advance in production rate cannot only be attributed to the higher density of active sites in the Rh-MOPs, as the *TOF* is also at least doubled. Recently, Fontecave and co-workers demonstrated that the redox potential of the active site in a series of $[Cp^*Rh(X\text{-}bpy)]^{2+}$ catalysts correlates directly with the Hammett constant of the substituent X on the bipyridine ligand,[51] and is thus a suitable descriptor for the change in electron density on the active site and subsequently in the catalytic activity. They observed that a lower redox potential, corresponding to a higher LUMO energy position, give rise to a higher catalytic activity, which they attributed, using DFT calculations, to a lower transition state barrier of the rate-limiting step. To elucidate the origin of the differences in catalytic activity, we determined the redox potential of the active site for molecular cluster models, *e.g.* the **C_{12}Rh-MOP**, **C_{12}Rh-MOP$_{bnix}$** and **HRh-MOP$_{bnix}$** as soluble model catalyst for our systems, and ([(5,5'-*bis*(phenylethinylene)-2,2'-bipyridine)(pentamethylcyclopentadienyl)rhodium] dichloride (Cp*Rh(*b*pe-bpy)Cl_2) as a soluble model catalyst for Cp*Rh@BpyMP-1. The Cp*Rh(*b*pe-bpy)Cl_2 molecular cluster model has been demonstrated to have the same electron density and thus the same catalytic activity as the corresponding heterogeneous catalyst.[9]

The electrochemical properties of the molecular clusters models were explored with cyclic voltammetry (for experimental details see SI, section 5). The cyclovoltammogram of **C_{12}Rh-MOP** indicates that the oxidation of the Rh_2 paddlewheel is reversible and occurs at approx. 0.64 V vs ferrocene/ferrocenium ($Fc^{+/0}$, -5.6 eV, Figure S17b). Upon addition of 12 equiv. bnix to simulate the linker surrounding the MOP in the solid materials,[36] the redox potential of the $Rh_2^{II,II}$/ $Rh_2^{II,III}$ redox couple in **C_{12}Rh-MOP$_{bnix}$** is shifted to approx. 0.52 V vs $Fc^{+/0}$ (-5.5 eV) and the oxidation becomes irreversible. This shift in redox potential was further supported by differential pulse voltammetry and is similarly observed for $Rh_2(OAc)_4$ (Figure S17a). Interestingly, no differences in the redox potential of the endohedral and exohedral axial Rh atom of the MOP were detected, indicating a strong electronic communication between the two Rh atoms. These observations are in line with the XPS investigations, showing also only one contribution for Rh in the oxidation state +II (Figure 2c). As the reduction of the Rh species cannot be detected by cyclic voltammetry,[10] we used the position of the $\pi^* \rightarrow \sigma^*$ transition of the Rh-Rh bond, determined from UV-vis spectroscopy (Figure S19), to calculate the LUMO energy level of the Rh-paddlewheel at -3.5 and -3.3 eV for **C_{12}Rh-MOP** and **C_{12}Rh-MOP$_{bnix}$** respectively (Figure 3b). For the **HRh-MOP$_{bnix}$** molecular cluster model the LUMO position is at

approx. -3.4 eV. Although we are aware that this procedure may overestimate the HOMO-LUMO-gap and thus place the estimated LUMO position at a higher energy position, we attempted to align frontier orbital positions with respect to the redox potential of the CO_2-to-formic acid transformation, to get insights into the thermodynamic driving forces. For the Cp*Rh(*b*pe-bpy)Cl_2 molecular clusters model, the cyclovoltammogram shows a reversible signal for the two electron reduction of the $Rh^{III/I}$ redox couple at approx. -1.06 V vs $Fc^{+/0}$ (-3.9 eV), corresponding to its LUMO position (HOMO-LUMO gap approx. 3.3 eV[52]). The higher LUMO position of the **C_{12}Rh-MOP$_{bnix}$** (-3.3 eV) as compared to the LUMO position of the **HRh-MOP$_{bnix}$** (-3.4 eV) is indicative of a higher electron density on Rh atoms in the $Rh_2^{II,II}$ paddlewheel, which explains the increased catalytic activity. The Cp*Rh(*b*pe-bpy)Cl_2 molecular cluster model shows the lowest LUMO position explaining also the lowest catalytic activity observed here, with *TOF*s up to 47 h^{-1} as compared to 58 h^{-1} for **C_{12}Rh-MOP$_{bnix}$** (Table S6, entries 2, 29 and Table S7, entries 1, 5).[51]

The redox potential of CO_2/HCOOH was calculated in acetonitrile following the procedure proposed by Mayer and co-workers[53] to be approx. 0.07 V vs $Fc^{+/0}$ (-5.05 eV, see SI).[53,54] Note that acetonitrile is an aprotic solvent, thus formic acid and not formate is the main product as the pK_a (20.9[55,56]) of formic acid is significantly higher than the pK_a of $TEOAH^+$ (calculated between 15.9[57] and 13.7[58]), which will be mainly deprotonated. We also considered the solvation and interaction of formic acid with triethanolamine using the following equation:

$$E^{\circ}_{CO_{2(g)}/HCO_2H_{(ACN)}} = 0.07\ \mathrm{V} - 0.059 \cdot \mathrm{p}K_a,^{55}$$

resulting in a redox potential range for CO_2/HCO_2H in ACN/TEOA between -4.10 and -4.24 eV. The thermodynamic driving force can be estimated from the energy difference ΔE between the redox potential $E^{\circ}_{CO_{2(g)}/HCO_2H_{(ACN)}}$ and the LUMO position of the molecular cluster model.[59] For the molecular model systems **HRh-MOP$_{bnix}$**, **C_{12}Rh-MOP** and **C_{12}Rh-MOP$_{bnix}$**, with LUMO positions at -3.4, -3.5 and -3.3 eV, the thermodynamic driving forces for CO_2 to formic acid reduction are approximately 670, 560 and 790 meV respectively, while the driving force is reduced to 180 meV in case of Cp*Rh(*b*pe-bpy)Cl_2. Thus by increasing the electron density on the Rh paddlewheel, bnix coordination results in a higher thermodynamic driving force for the reaction, most likely by a reduced energy barrier for the rate-limiting step,[51] explaining the observed higher catalytic activities in **C_{12}Rh-CPP** and **C_{12}Rh-SAG** materials (Figure S21). This finding is in line with our recent work on molecular catalysts in microporous materials and the design of the catalytic activity by tailoring the Hammett constants of the metal ligands and subsequently the electron density on the active metal site.[9]

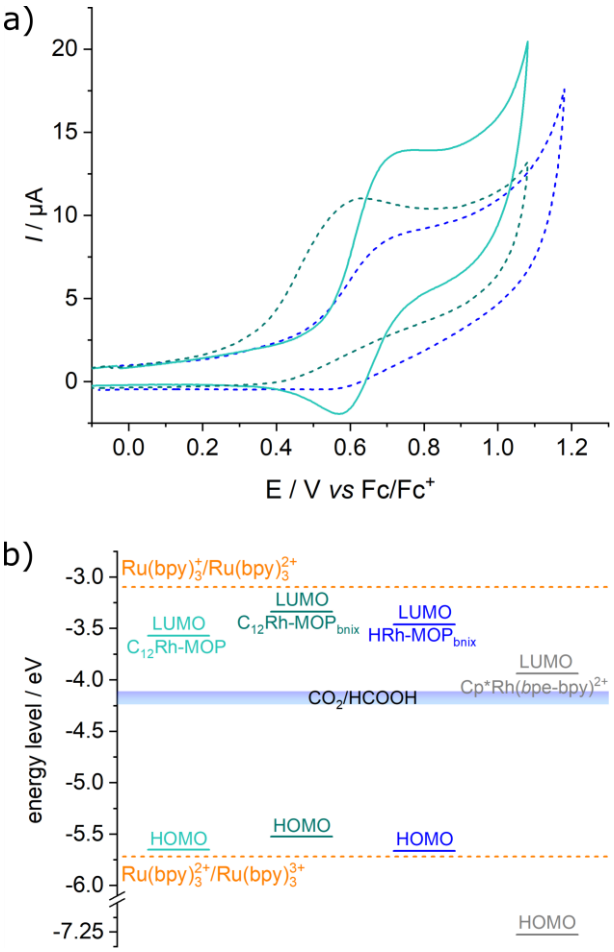

Figure 3. a) Cyclovoltammogram of **C_{12}Rh-MOP** (light turquoise), **C_{12}Rh-MOP$_{bnix}$** (dark turquoise) and **HRh-MOP$_{bnix}$** (blue) in DMF containing 0.1 M Bu_4NPF_6 using a glassy carbon working electrode at a scan rate of 100 mV·s^{-1}. b) Diagram of HOMO and LUMO energy levels of **C_{12}Rh-MOP** (light turquoise), **C_{12}Rh-MOP$_{bnix}$** (dark turquoise), **HRh-MOP$_{bnix}$** (blue) and Cp*Rh(*b*pe-bpy)$^{2+}$ (gray) together with redox potentials in eV for formic acid production in acetonitrile (taking also the solvation effect of TEOA and its pK_a into account to calculate the appropriate potential range).

Recycling experiments. Recycling tests were conducted using the most active heterogeneous catalyst **C_{12}Rh-CPP** to demonstrate the heterogeneous nature of the catalyst. After 2 h of photocatalysis, the catalyst was isolated, washed, dried under vacuum and used for up to 4 cycles (Figure 4, Table S6, entry 20 – 23, see SI for further details). The catalytic activity seemingly increased slightly, but the variation is within the standard deviation and is therefore assumed to be constant. In addition, long term experiments were carried out to understand the stability of the catalyst during several hours of continuous irradiation. After two hours of catalysis, the catalytic activity started to decrease from ~53 h^{-1} to ~22 h^{-1} after 8 hours of catalysis (Table S6 entries 4 – 7). The initial level of catalytic activity could be recovered by adding fresh solution of $Ru(bpy)_3Cl_2$ after 2, 4 and 6 hours of catalysis (Figure 4b, see SI section 6.1 for further details, Table S6 entries 8 – 19).[47,60] Here we note that the initial catalytic activity was retained if at least the

initial molar amount of $Ru(bpy)_3Cl_2$ was added after each step, indicating that most of the photosensitizer was decomposed within two hours. Thus, both recycling and long-term experiments highlight the stable catalytic activity.

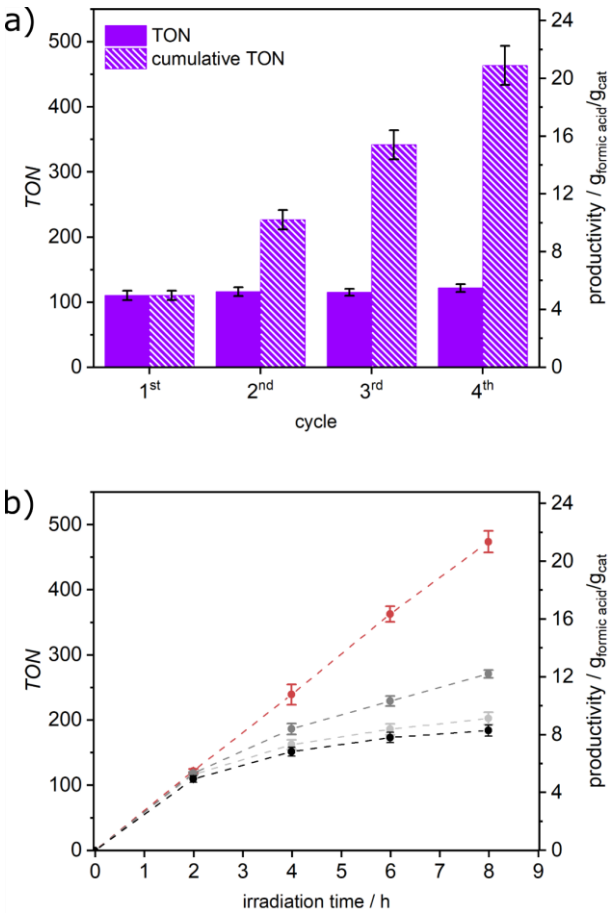

Figure 4. a) Catalytic activity over four cycles of catalysis using **C_{12}Rh-CPP** (~1.1 µmol) in the presence of $Ru(bpy)_3Cl_2$ (21.2 µmol, 1 equiv) as photosensitizer in ACN / TEOA (4 : 1, *V* : *V*), 2h. After each run the solid was isolated by centrifugation, washed and reused with a fresh solution of $Ru(bpy)_3Cl_2$. b) Comparison of TON and productivity for continuous photocatalytic experiments where different amounts of $Ru(bpy)_3Cl_2$ were added after 2, 4 and 6 h. 0 equiv. (black), 0.025 equiv (light grey), 0.25 equiv (grey) and 1 equiv of the initial amount of $Ru(bpy)_3Cl_2$ added.

Importantly, the structural properties of fresh and spent **C_{12}Rh-CPP** remain unchanged (Figure 5, and SI section 6.2). TEM analysis indicate no change of the particle morphology (Figure 5a, b). The powder X-ray diffraction (PXRD) patterns of fresh and spent catalyst are not distinguishable, featuring broad peaks at low diffraction angles, indicative of a partial long-range ordering in the materials (Figure 5c). Importantly no changes in the relative signal intensities and full width at half maximum are observed, excluding any loss in crystallinity or amorphization to occur during catalysis. XPS spectra after one cycle of photocatalysis reveal no changes of the organic backbone of the material but significant changes of the electron binding energy on the catalytically active Rh sites (Figure 5d). After catalysis, the main signal (~75% of surface species) is centred at 309 eV with a minor contribution from reduced species (~25% of surface species) visible as a small shoulder at 307.4 eV, which is most likely attributed to Rh^0.[61] A reduction into crystalline metallic Rh is excluded by PXRD, as no additional peaks are observed after catalysis (Figure 5c) and no Rh nanoparticles are observed by TEM analysis (Figure 5a, b, Figures S24, S25). However, the formation of amorphous Rh^0 clusters cannot be excluded from TEM analysis alone.

PDF analysis and molecular structure of the active site. To obtain insights into the precise molecular ordering around the active site after MOP incorporation into the supramolecular polymers, we performed pair distribution function analysis (PDF).[62–66] PDF provides local structural information such as inter-atomic distances between atoms even from amorphous materials,[67] and has been recently shown to be a powerful technique to assess the post-catalytic structural integrity of molecular components of complex catalysts.[47] Hence, we aimed to reveal possible structural changes after catalysis, as well as the nature of the Rh^0 species observed by XPS analysis (Figure 5d). Interestingly, the PDFs of fresh and spent **C_{12}Rh-CPP** and **C_{12}Rh-SAG** catalysts display similar features up to 22 Å, with only slight differences in peak position and intensity (SI section S4, Figure S16). We here focus on the short distances up to 11 Å (Figure 5e, f). The peak at approx. 1.5 Å can be attributed to C-C bonds. Peaks at higher distances were assigned using the single crystal structure of the pristine **HRh-MOP**.[37] Peaks at 2.0 and 2.39 Å can be attributed to Rh-O and Rh-Rh distances within one paddlewheel, respectively. The diffusion factor of rhodium being stronger than those of other involved atoms of Rh-MOPs, most of the peaks seen here emanate from Rh-based pairs (distances between carbons atoms across several C-C bonds are hidden). Peaks in the region 2.9 – 7 Å can thus be assigned to distances between one Rh atom and one C or O atom from the BDC ligands within the Rh_2 paddlewheel unit, while peaks between 7.9 and 10.7 Å can be assigned to Rh-Rh distances between two neighbouring paddle wheel units in the **C_{12}Rh-MOP** cuboctahedral architecture. The similarity of the pristine and spent *G*(*r*) curves demonstrates that at the molecular level, no decomposition or distortion of the active Rh paddlewheel sites occurs after catalysis for **C_{12}Rh-CPP** and **C_{12}Rh-SAG**. This stability during catalysis is also highlighted by the clear absence of a peak at 2.7 Å, that would have shown the formation of metallic Rh or Rh^0 clusters and would indicate unwanted reductive decomposition of the Rh_2 paddlewheel.[68,69] Thus, PDF analysis provides strong evidence that the Rh^0 resting state observed by XPS analysis is located in a reduced $[Rh_2^{II,0}]$ or $[Rh_2^{0,0}]$ paddlewheel, but not caused by the formation of Rh^0 clusters.

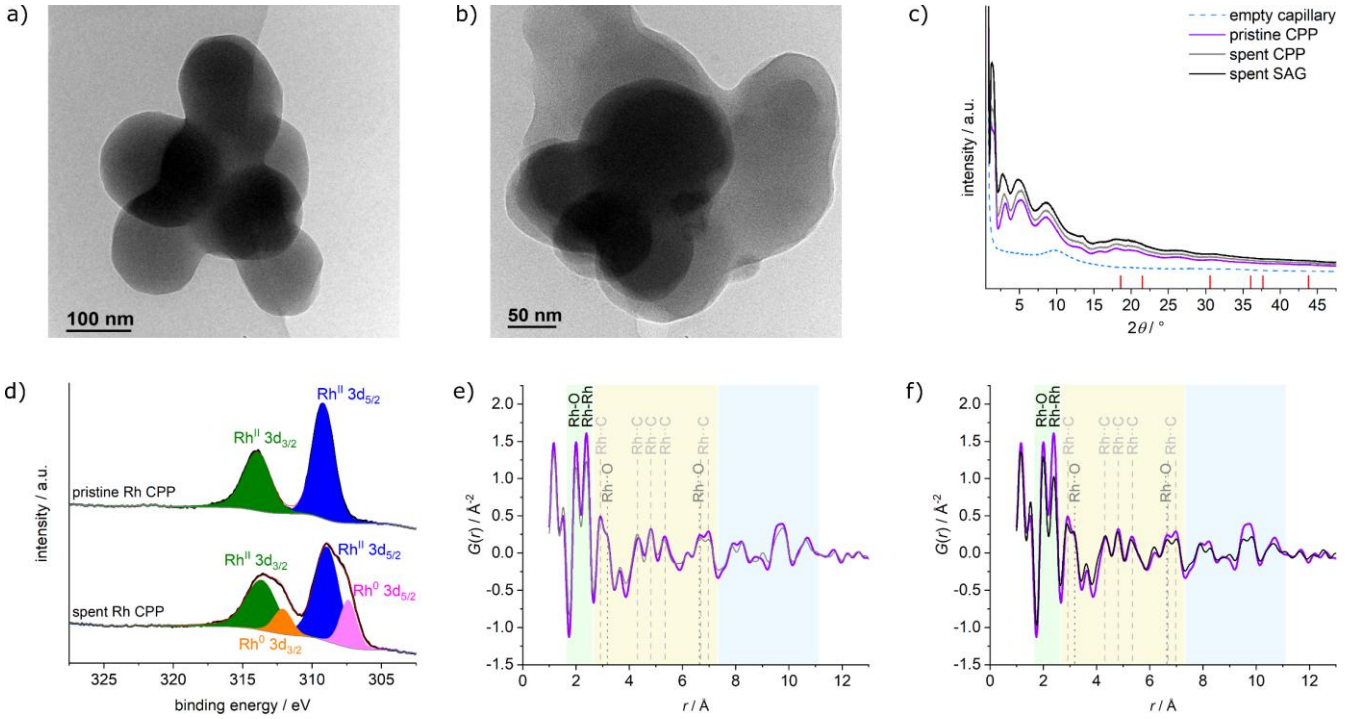

Figure 5. TEM image of a) fresh and b) spent C_{12}Rh-CPP. c) Powder XRD pattern of pristine **C_{12}Rh-CPP** (purple), spent **C_{12}Rh-CPP** catalyst (gray) and spent **C_{12}Rh-SAG** catalyst (black) measured using Mo K_α radiation. Bragg marker: Rh (red), COD 9008482, calculated for Mo K_α radiation. d) XPS spectra of fresh and spent catalyst including deconvolution of the signals. On the surface, 25% of the Rh atoms are reduced to most likely Rh^0 species. e) PDF analysis: G(r) curve of pristine **C_{12}Rh-CPP** (purple) and spent **C_{12}Rh-CPP** catalyst (grey) and f) G(r) curve PDF of pristine **C_{12}Rh-CPP** (purple) and spent **C_{12}Rh-SAG** catalyst (black). Interatomic distances within the Rh_2O_8-moiety are highlighted in green, within the Rh_2 paddlewheel unit and including the benzene dicarboxylic acid (bdc) ligands in yellow and neighboring paddlewheels in blue.

In summary, the combined XPS and PDF investigation of spent catalysts exclude any degradation into Rh^0 clusters or particles,[70] or into unimolecular or polymeric Rh^I species,[71–73] which, in contrast, was observed in the case of photocatalysis with $[Rh_2(OAc)_4]$ as catalyst (Figure S24b) and has been reported for different molecular $Rh_2^{II,II}$ carboxylates.[70–73] Thus the fixation of the Rh_2 paddlewheel into a solid scaffold prevents these undesired side reactions.[16] Moreover, X-ray fluorescence spectroscopy and ICP OES analysis of the supernatant confirms that no quantifiable leaching of Rh occurs (< 5 ppm).

Catalytic cycle. To shine light onto the photo-induced activation of $Rh_2^{II,II}$ paddlewheel, EPR studies under illumination were conducted on the molecular Rh-MOPs in the presence of $Ru(bpy)_3Cl_2$. Upon irradiation of a solution of $[Ru^{II}(bpy)_3]^{2+}$ in ACN/TEOA mixture, the photo-excited $[Ru^{II}(bpy)_3]^{2+*}$ is reductively quenched by reaction with TEOA yielding the $[Ru^{II}(bpy)_3]^{\bullet+}$ radical cation with the characteristic EPR signal at approx. *g* = 2.00 for a bipyridine centred radical (Figure S28). The signal of the reduced radical $[Ru^{II}(bpy)_3]^{\bullet+}$ species is efficiently quenched upon addition of Rh-MOP to the solution (Figure S28). No signal of a reduced $Rh_2^{II,I}$ paddlewheel species can be observed with *g*-values well above 2,[70,73,74] in line with the XPS investigation of spent catalysts highlighting a Rh^0 resting state (Figure 2c) as well as the electrochemical investigations (Figure 3). Combining the results from XPS, EPR and electro chemical characterization, we postulate a reaction mechanism that involves (i) the photoexcitation and reductive quenching of the $[Ru^{II}(bpy)_3]^{2+}$ photosensitizer by TEOA to yield $[Ru^{II}(bpy)_3]^{\bullet+}$, then (ii) electron transfer from the reduced photosensitizer $[Ru^{II}(bpy)_3]^{\bullet+}$ to the Rh catalyst and followed by (iii) the reduction of CO_2 into formic acid (Figure S29).[11,60,75] The required protons for the formic acid formation most likely stem from proton abstraction from the nitrogen centred $TEOA^{\bullet+}$ radical to yield a carbon centred radical, which is a much stronger reductant, capable of transferring a second electron as well as a second proton and thus avoiding back electron transfer.[76–78]

CONCLUSION

We investigated Rh_2 paddlewhee-based cuboctahedral metal-organic polyhedra, Rh-MOP, both molecularly and self-assembled into supramolecular polymers colloidal particle (Rh-CPP) and colloidal aerogel (Rh-SAG) as well as $[Rh_3BTC_2]_n$ (Rh-MOF) for photocatalytic CO_2 reduction. The heterogenized supramolecular catalysts showed extraordinary turnover frequencies of up to 60 h^{-1}, corresponding to production rates of approx. 2.7 $g_{formic\ acid}/g_{cat}/h$, outperforming the molecular Rh-MOP catalysts by up to 30 % and state-of-the-art heterogeneous photocatalysts, including Rh-MOF, by at least a factor of twelve. The very high catalytic activity compared to other heterogeneous photocatalysts can be rationalized by the high number of Rh sites per gram of catalyst, but also by their very high accessibility inside the supramolecular cage. Importantly, we were able to show, by pair distribu-

tion function analysis, that all Rh is coordinated in molecular cages and that no formation of colloidal Rh^0 or Rh nanoparticles occurs, indicating the high stability of these heterogeneous catalysts. This is confirmed by recycling tests of at least 4 cycles without any loss of activity. The coordination of the MOP by electron-donating N-ligands not only leads to a heterogenization of the active centre in a stable, and easily recyclable polymer. XPS spectroscopy and electrochemical characterization also show that the N-ligands increases the electron density at the active Rh site compared to the molecular catalyst in solution, leading to a higher thermodynamic driving force of the reaction. This finding is in line with our recent works on molecular catalysts in microporous materials and the design of the catalytic activity by tailoring the Hammett constants of the metal ligands.

The present work demonstrates the high potential of MOP and of their polymer derivatives as catalysts for the photoreduction of CO_2 with unprecedented efficiency and opens new perspectives for the electronic design of novel discrete molecular architectures with accessible metal sites for the production of solar fuels.

ASSOCIATED CONTENT

Supporting Information. Detailed experimental procedures, materials and instruments used as well as addition material characterization and overview are provided in the Supporting Information.

AUTHOR INFORMATION

Corresponding Author

* florian.wisser@ur.de, jerome.canivet@ircelyon.univ-lyon1.fr, shuhei.furukawa@icems.kyoto-u.ac.jp

ORCID

Ashta C. Ghosh: 0000-0003-3137-6580
Alexandre Legrand: 0000-0002-7975-9348
Gavin A. Craig: 0000-0003-3542-4850
Zahraa Shahin: 0000-0002-4210-2801
Capucine Sassoye: 0000-0003-2790-888X
Gabor Balazs: 0000-0003-3497-7082
David Farrusseng: 0000-0002-9093-4143
Shuhei Furukawa: 0000-0003-3849-8038
Jérôme Canivet: 0000-0002-0458-3085
Florian M. Wisser: 0000-0002-5925-895X

Present Addresses

♦ University of Strathclyde, Department of Pure and Applied Chemistry.

Author Contributions

$^{\Delta}$ A.C.G. and A.L. contributed equally. The manuscript was written through contributions of all authors. All authors have given approval to the final version of the manuscript.

ACKNOWLEDGMENT

The authors are grateful to Caroline Mellot-Draznieks for fruitful discussion of PDF data. F.M.W. gratefully acknowledges financial support from the Deutsche Forschungsgemeinschaft (DFG, grant number WI 4721/3-1). F.M.W. and A.C.G. acknowledge financial support from CNRS through Momentum 2018 excellence grant. D.F. and J.C. acknowledge financial support from the CNRS International Research Project “Small Molecule Lab: IRP-Smolab”. This study was supported by JSPS KAKENHI Grant Number 20K15366 (Wakate) for A.L. and 19H04575 (Coordination Asymmetry) and 18H01995 (Kiban B) for S.F. The authors thank the iCeMS Analysis Center for access to analytical instruments. The authors are very grateful to H. Izu for the access to the electrochemistry device, P. Mascunan for ICP-OES, N. Bonnet for XRF analysis and P. P. Bargiela for XPS analysis.

REFERENCES

(1) Cui, X.; Li, W.; Ryabchuk, P.; Junge, K.; Beller, M. Bridging Homogeneous and Heterogeneous Catalysis by Heterogeneous Single-Metal-Site Catalysts. *Nat. Catal.* **2018**, *1* (6), 385–397. https://doi.org/10.1038/s41929-018-0090-9.

(2) Drake, T.; Ji, P.; Lin, W. Site Isolation in Metal-Organic Frameworks Enables Novel Transition Metal Catalysis. *Acc. Chem. Res.* **2018**, *51* (9), 2129–2138. https://doi.org/10.1021/acs.accounts.8b00297.

(3) Copéret, C.; Comas-Vives, A.; Conley, M. P.; Estes, D. P.; Fedorov, A.; Mougel, V.; Nagae, H.; Núnez-Zarur, F.; Zhizhko, P. A. Surface Organometallic and Coordination Chemistry toward Single-Site Heterogeneous Catalysts: Strategies, Methods, Structures, and Activities. *Chem. Rev.* **2016**, *116* (2), 323–421. https://doi.org/10.1021/acs.chemrev.5b00373.

(4) Copéret, C.; Fedorov, A.; Zhizhko, P. A. Surface Organometallic Chemistry: Paving the Way Beyond Well-Defined Supported Organometallics and Single-Site Catalysis. *Catal. Letters* **2017**, *147* (9), 2247–2259. https://doi.org/10.1007/s10562-017-2107-4.

(5) Wisser, F. M.; Mohr, Y.; Quadrelli, E. A.; Canivet, J. Porous Macroligands: Materials for Heterogeneous Molecular Catalysis. *ChemCatChem* **2020**, *12* (5), 1270–1275. https://doi.org/10.1002/cctc.201902064.

(6) Qiao, B.; Wang, A.; Yang, X.; Allard, L. F.; Jiang, Z.; Cui, Y.; Liu, J.; Li, J.; Zhang, T. Single-Atom Catalysis of CO Oxidation Using Pt1/FeOx. *Nat. Chem.* **2011**, *3* (8), 634–641. https://doi.org/10.1038/nchem.1095.

(7) Quadrelli, E. A.; Basset, J. M. On Silsesquioxanes' Accuracy as Molecular Models for Silica-Grafted Complexes in Heterogeneous Catalysis. *Coord. Chem. Rev.* **2010**, *254* (5–6), 707–728. https://doi.org/10.1016/j.ccr.2009.09.031.

(8) Conley, M. P.; Copéret, C. State of the Art and Perspectives in the “Molecular Approach” towards Well-Defined Heterogeneous Catalysts. *Top. Catal.* **2014**, *57* (10–13), 843–851. https://doi.org/10.1007/s11244-014-0245-0.

(9) Wisser, F. M.; Berruyer, P.; Cardenas, L.; Mohr, Y.; Quadrelli, E. A.; Lesage, A.; Farrusseng, D.; Canivet, J. Hammett Parameter in Microporous Solids as Macroligands for Heterogenized Photocatalysts. *ACS Catal.* **2018**, *8* (3), 1653–1661. https://doi.org/10.1021/acscatal.7b03998.

(10) Chinapang, P.; Okamura, M.; Itoh, T.; Kondo, M.; Masaoka, S. Development of a Framework Catalyst for Photocatalytic Hydrogen Evolution. *Chem. Commun.* **2018**, *54* (10), 1174–1177. https://doi.org/10.1039/c7cc08013a.

(11) Lin, S.; Turro, C. Dirhodium Complexes as Panchromatic Sensitizers, Electrocatalysts, and Photocatalysts. *Chem. – A Eur. J.* **2021**, *27* (17), 5379–5387. https://doi.org/10.1002/chem.202003950.

(12) Kumar, D. K.; Filatov, A. S.; Napier, M.; Sun, J.; Dikarev, E. V.; Petrukhina, M. A. Dirhodium Paddlewheel with Functionalized Carboxylate Bridges: New Building Block for Self-Assembly and Immobilization on Solid Support. *Inorg. Chem.* **2012**, *51* (8), 4855–4861. https://doi.org/10.1021/ic300382j.

(13) Liu, J.; Fasel, C.; Braga-Groszewicz, P.; Rothermel, N.;

Lilly Thankamony, A. S.; Sauer, G.; Xu, Y.; Gutmann, T.; Buntkowsky, G. Heterogeneous Self-Supported Dirhodium(II) Catalysts with High Catalytic Efficiency in Cyclopropanation-a Structural Study. *Catal. Sci. Technol.* **2016**, *6* (21), 7830–7840. https://doi.org/10.1039/C6CY00915H.

(14) Mori, W.; Takamizawa, S.; Kato, C. N.; Ohmura, T.; Sato, T. Molecular-Level Design of Efficient Microporous Materials Containing Metal Carboxylates: Inclusion Complex Formation with Organic Polymer, Gas-Occlusion Properties, and Catalytic Activities for Hydrogenation of Olefins. *Microporous Mesoporous Mater.* **2004**, *73* (1–2), 31–46. https://doi.org/10.1016/j.micromeso.2004.02.019.

(15) Sato, T.; Mori, W.; Kato, C. N.; Yanaoka, E.; Kuribayashi, T.; Ohtera, R.; Shiraishi, Y. Novel Microporous Rhodium(II) Carboxylate Polymer Complexes Containing Metalloporphyrin: Syntheses and Catalytic Performances in Hydrogenation of Olefins. *J. Catal.* **2005**, *232* (1), 186–198. https://doi.org/10.1016/j.jcat.2005.02.007.

(16) Shakya, D. M.; Ejegbavwo, O. A.; Rajeshkumar, T.; Senanayake, S. D.; Brandt, A. J.; Farzandh, S.; Acharya, N.; Ebrahim, A. M.; Frenkel, A. I.; Rui, N.; Tate, G. L.; Monnier, J. R.; Vogiatzis, K. D.; Shustova, N. B.; Chen, D. A. Selective Catalytic Chemistry at Rhodium(II) Nodes in Bimetallic Metal–Organic Frameworks. *Angew. Chem. Int. Ed.* **2019**, *58* (46), 16533–16537. https://doi.org/10.1002/anie.201908761.

(17) Nickerl, G.; Stoeck, U.; Burkhardt, U.; Senkovska, I.; Kaskel, S. A Catalytically Active Porous Coordination Polymer Based on a Dinuclear Rhodium Paddle-Wheel Unit. *J. Mater. Chem. A* **2014**, *2* (1), 144–148. https://doi.org/10.1039/c3ta12795h.

(18) Heinz, W. R.; Agirrezabal-Telleria, I.; Junk, R.; Berger, J.; Wang, J.; Sharapa, D. I.; Gil-Calvo, M.; Luz, I.; Soukri, M.; Studt, F.; Wang, Y.; Wöll, C.; Bunzen, H.; Drees, M.; Fischer, R. A. Thermal Defect Engineering of Precious Group Metal–Organic Frameworks: A Case Study on Ru/Rh-HKUST-1 Analogues. *ACS Appl. Mater. Interfaces* **2020**, *12* (36), 40635–40647. https://doi.org/10.1021/acsami.0c10721.

(19) Stoll, T.; Castillo, C. E.; Kayanuma, M.; Sandroni, M.; Daniel, C.; Odobel, F.; Fortage, J.; Collomb, M. N. Photo-Induced Redox Catalysis for Proton Reduction to Hydrogen with Homogeneous Molecular Systems Using Rhodium-Based Catalysts. *Coord. Chem. Rev.* **2015**, *304–305*, 20–37. https://doi.org/10.1016/j.ccr.2015.02.002.

(20) Kataoka, Y.; Sato, K.; Miyazaki, Y.; Suzuki, Y.; Tanaka, H.; Kitagawa, Y.; Kawakami, T.; Okumura, M.; Mori, W. Photocatalytic Hydrogen Production from Water Using Heterogeneous Two-Dimensional Rhodium Coordination Polymer [Rh2(p-BDC) 2]N. *Chem. Lett.* **2010**, *39* (4), 358–359. https://doi.org/10.1246/cl.2010.358.

(21) Bavykina, A.; Cadiau, A.; Gascon, J. Porous Liquids Based on Porous Cages, Metal Organic Frameworks and Metal Organic Polyhedra. *Coord. Chem. Rev.* **2019**, *386*, 85–95. https://doi.org/10.1016/j.ccr.2019.01.015.

(22) Hasell, T.; Schmidtmann, M.; Cooper, A. I. Molecular Doping of Porous Organic Cages. *J. Am. Chem. Soc.* **2011**, *133* (38), 14920–14923. https://doi.org/10.1021/ja205969q.

(23) Sharma, V.; De, D.; Saha, R.; Chattaraj, P. K.; Bharadwaj, P. K. Flexibility Induced Encapsulation of Ultrafine Palladium Nanoparticles into Organic Cages for Tsuji-Trost Allylation. *ACS Appl. Mater. Interfaces* **2020**, *12* (7), 8539–8546. https://doi.org/10.1021/acsami.9b19480.

(24) Vardhan, H.; Yusubov, M.; Verpoort, F. Self-Assembled Metal–Organic Polyhedra: An Overview of Various Applications. *Coord. Chem. Rev.* **2016**, *306* (P1), 171–194. https://doi.org/10.1016/j.ccr.2015.05.016.

(25) Dechnik, J.; Gascon, J.; Doonan, C. J.; Janiak, C.; Sumby, C. J. Mixed-Matrix Membranes. *Angew. Chem. Int. Ed.* **2017**, *56* (32), 9292–9310. https://doi.org/10.1002/anie.201701109.

(26) Hosono, N.; Kitagawa, S. Modular Design of Porous Soft Materials via Self-Organization of Metal–Organic Cages. *Acc. Chem. Res.* **2018**, *51* (10), 2437–2446. https://doi.org/10.1021/acs.accounts.8b00361.

(27) Gosselin, A. J.; Rowland, C. A.; Bloch, E. D. Permanently Microporous Metal–Organic Polyhedra. *Chem. Rev.* **2020**, *120* (16), 8987–9014. https://doi.org/10.1021/acs.chemrev.9b00803.

(28) Vardhan, H.; Verpoort, F. Metal-Organic Polyhedra: Catalysis and Reactive Intermediates. *Adv. Synth. Catal.* **2015**, *357* (7), 1351–1368. https://doi.org/10.1002/adsc.201400778.

(29) Tan, C.; Jiao, J.; Li, Z.; Liu, Y.; Han, X.; Cui, Y. Design and Assembly of a Chiral Metallosalen-Based Octahedral Coordination Cage for Supramolecular Asymmetric Catalysis. *Angew. Chem. Int. Ed.* **2018**, *57* (8), 2085–2090. https://doi.org/10.1002/anie.201711310.

(30) Lee, H. S.; Jee, S.; Kim, R.; Bui, H.-T.; Kim, B.; Kim, J.-K.; Park, K. S.; Choi, W.; Kim, W.; Choi, K. M. A Highly Active, Robust Photocatalyst Heterogenized in Discrete Cages of Metal–Organic Polyhedra for CO 2 Reduction. *Energy Environ. Sci.* **2020**, *13* (2), 519–526. https://doi.org/10.1039/C9EE02619C.

(31) Lee, S.; Jeong, H.; Nam, D.; Lah, M. S.; Choe, W. The Rise of Metal–Organic Polyhedra. *Chem. Soc. Rev.* **2021**, *50* (1), 528–555. https://doi.org/10.1039/D0CS00443J.

(32) Ji, C.; Wang, W.; El-Sayed, E.-S. M.; Liu, G.; Si, Y.; Su, K.; Ju, Z.; Wu, F.; Yuan, D. A High-Efficiency Dye-Sensitized Pt(II) Decorated Metal-Organic Cage for Visible-Light-Driven Hydrogen Production. *Appl. Catal. B Environ.* **2021**, *285*, 119782. https://doi.org/10.1016/j.apcatb.2020.119782.

(33) Chen, L.; Yang, T.; Cui, H.; Cai, T.; Zhang, L.; Su, C.-Y. A Porous Metal–Organic Cage Constructed from Dirhodium Paddle-Wheels: Synthesis, Structure and Catalysis. *J. Mater. Chem. A* **2015**, *3* (40), 20201–20209. https://doi.org/10.1039/C5TA05592J.

(34) Kang, Y.-H.; Liu, X.-D.; Yan, N.; Jiang, Y.; Liu, X.-Q.; Sun, L.-B.; Li, J.-R. Fabrication of Isolated Metal–Organic Polyhedra in Confined Cavities: Adsorbents/Catalysts with Unusual Dispersity and Activity. *J. Am. Chem. Soc.* **2016**, *138* (19), 6099–6102. https://doi.org/10.1021/jacs.6b01207.

(35) Zhang, Z.; Lei, Y.; Zhou, J.; Cui, M.; Chen, X.; Fei, Z.; Liu, Q.; Tang, J.; Qiao, X. Simultaneous Shaping and Confinement of Metal–Organic Polyhedra in Alginate-SiO 2 Spheres. *Chem. Commun.* **2020**, *56* (94), 14833–14836. https://doi.org/10.1039/D0CC05619G.

(36) Carné-Sánchez, A.; Craig, G. A.; Larpent, P.; Hirose, T.; Higuchi, M.; Kitagawa, S.; Matsuda, K.; Urayama, K.; Furukawa, S. Self-Assembly of Metal–Organic Polyhedra into Supramolecular Polymers with Intrinsic Microporosity. *Nat. Commun.* **2018**, *9* (1), 2506. https://doi.org/10.1038/s41467-018-04834-0.

(37) Furukawa, S.; Horike, N.; Kondo, M.; Hijikata, Y.; Carné-Sánchez, A.; Larpent, P.; Louvain, N.; Diring, S.; Sato, H.; Matsuda, R.; Kawano, R.; Kitagawa, S. Rhodium-Organic Cuboctahedra as Porous Solids with Strong Binding Sites. *Inorg. Chem.* **2016**, *55* (21), 10843–10846. https://doi.org/10.1021/acs.inorgchem.6b02091.

(38) Miklitz, M.; Jelfs, K. E. Pywindow : Automated Structural Analysis of Molecular Pores. *J. Chem. Inf. Model.* **2018**, *58* (12), 2387–2391. https://doi.org/10.1021/acs.jcim.8b00490.

(39) Kawano, R.; Horike, N.; Hijikata, Y.; Kondo, M.; Carné-Sánchez, A.; Larpent, P.; Ikemura, S.; Osaki, T.; Kamiya, K.; Kitagawa, S.; Takeuchi, S.; Furukawa, S. Metal-Organic Cuboctahedra for Synthetic Ion Channels with Multiple Conductance States. *Chem* **2017**, *2* (3), 393–403. https://doi.org/10.1016/j.chempr.2017.02.002.

(40) Heinz, W. R.; Kratky, T.; Drees, M.; Wimmer, A.; Tomanec, O.; Günther, S.; Schuster, M.; Fischer, R. A. Mixed Precious-Group Metal–Organic Frameworks: A Case Study of the HKUST-1 Analogue [Ru x Rh 3−x (BTC) 2]. *Dalt. Trans.* **2019**, *48* (32), 12031–12039. https://doi.org/10.1039/C9DT01198F.

(41) Carné-Sánchez, A.; Craig, G. A.; Larpent, P.; Guillerm, V.;

Urayama, K.; Maspoch, D.; Furukawa, S. A Coordinative Solubilizer Method to Fabricate Soft Porous Materials from Insoluble Metal–Organic Polyhedra. *Angew. Chem. Int. Ed.* **2019**, *58* (19), 6347–6350. https://doi.org/10.1002/anie.201901668.

(42) Hansch, C.; Leo, A.; Taft, R. W. A Survey of Hammett Substituent Constants and Resonance and Field Parameters. *Chem. Rev.* **1991**, *91* (2), 165–195. https://doi.org/10.1021/cr00002a004.

(43) Vermoortele, F.; Vandichel, M.; Van De Voorde, B.; Ameloot, R.; Waroquier, M.; Van Speybroeck, V.; De Vos, D. E. Electronic Effects of Linker Substitution on Lewis Acid Catalysis with Metal-Organic Frameworks. *Angew. Chem. Int. Ed.* **2012**, *51* (20), 4887–4890. https://doi.org/10.1002/anie.201108565.

(44) Lee, Y.; Kim, S.; Fei, H.; Kang, J. K.; Cohen, S. M. Photocatalytic CO $_2$ Reduction Using Visible Light by Metal-Monocatecholato Species in a Metal–Organic Framework. *Chem. Commun.* **2015**, *51* (92), 16549–16552. https://doi.org/10.1039/C5CC04506A.

(45) Sun, D.; Gao, Y.; Fu, J.; Zeng, X.; Chen, Z.; Li, Z. Construction of a Supported Ru Complex on Bifunctional MOF-253 for Photocatalytic CO2 Reduction under Visible Light. *Chem. Commun.* **2015**, *51* (13), 2645–2648. https://doi.org/10.1039/c4cc09797a.

(46) Kajiwara, T.; Fujii, M.; Tsujimoto, M.; Kobayashi, K.; Higuchi, M.; Tanaka, K.; Kitagawa, S. Photochemical Reduction of Low Concentrations of CO2 in a Porous Coordination Polymer with a Ruthenium(II)-CO Complex. *Angew. Chem. Int. Ed.* **2016**, *55* (8), 2697–2700. https://doi.org/10.1002/anie.201508941.

(47) Benseghir, Y.; Lemarchand, A.; Duguet, M.; Mialane, P.; Gomez-Mingot, M.; Roch-Marchal, C.; Pino, T.; Ha-Thi, M. H.; Haouas, M.; Fontecave, M.; Dolbecq, A.; Sassoye, C.; Mellot-Draznieks, C. Co-Immobilization of a Rh Catalyst and a Keggin Polyoxometalate in the UiO-67 Zr-Based Metal-Organic Framework: In Depth Structural Characterization and Photocatalytic Properties for CO2 Reduction. *J. Am. Chem. Soc.* **2020**, *142* (20), 9428–9438. https://doi.org/10.1021/jacs.0c02425.

(48) Kuriki, R.; Matsunaga, H.; Nakashima, T.; Wada, K.; Yamakata, A.; Ishitani, O.; Maeda, K. Nature-Inspired, Highly Durable CO2 Reduction System Consisting of a Binuclear Ruthenium(II) Complex and an Organic Semiconductor Using Visible Light. *J. Am. Chem. Soc.* **2016**, *138* (15), 5159–5170. https://doi.org/10.1021/jacs.6b01997.

(49) Cauwenbergh, R.; Das, S. Photochemical Reduction of Carbon Dioxide to Formic Acid. *Green Chem.* **2021**, *23* (7), 2553–2574. https://doi.org/10.1039/D0GC04040A.

(50) Woo, S.-J.; Choi, S.; Kim, S.-Y.; Kim, P. S.; Jo, J. H.; Kim, C. H.; Son, H.-J.; Pac, C.; Kang, S. O. Highly Selective and Durable Photochemical CO 2 Reduction by Molecular Mn(I) Catalyst Fixed on a Particular Dye-Sensitized TiO 2 Platform. *ACS Catal.* **2019**, *9* (3), 2580–2593. https://doi.org/10.1021/acscatal.8b03816.

(51) Todorova, T. K.; Huan, T. N.; Wang, X.; Agarwala, H.; Fontecave, M. Controlling Hydrogen Evolution during Photoreduction of CO 2 to Formic Acid Using [Rh(R-Bpy)(Cp*)Cl] + Catalysts: A Structure–Activity Study. *Inorg. Chem.* **2019**, *58* (10), 6893–6903. https://doi.org/10.1021/acs.inorgchem.9b00371.

(52) Oppelt, K.; Egbe, D. A. M.; Monkowius, U.; List, M.; Zabel, M.; Sariciftci, N. S.; Knör, G. Luminescence and Spectroscopic Studies of Organometallic Rhodium and Rhenium Multichromophore Systems Carrying Polypyridyl Acceptor Sites and Phenylethynyl Antenna Subunits. *Journal of Organometallic Chemistry*. 2011, pp 2252–2258. https://doi.org/10.1016/j.jorganchem.2010.11.008.

(53) Pegis, M. L.; Roberts, J. A. S.; Wasylenko, D. J.; Mader, E. A.; Appel, A. M.; Mayer, J. M. Standard Reduction Potentials for Oxygen and Carbon Dioxide Couples in Acetonitrile and N,N-Dimethylformamide. *Inorg. Chem.* **2015**, *54* (24), 11883–11888. https://doi.org/10.1021/acs.inorgchem.5b02136.

(54) Johnson, S. I.; Nielsen, R. J.; Goddard, W. A. Selectivity for HCO 2 – over H 2 in the Electrochemical Catalytic Reduction of CO 2 by (POCOP)IrH 2. *ACS Catal.* **2016**, *6* (10), 6362–6371. https://doi.org/10.1021/acscatal.6b01755.

(55) Waldie, K. M.; Ostericher, A. L.; Reineke, M. H.; Sasayama, A. F.; Kubiak, C. P. Hydricity of Transition-Metal Hydrides: Thermodynamic Considerations for CO2 Reduction. *ACS Catal.* **2018**, *8* (2), 1313–1324. https://doi.org/10.1021/acscatal.7b03396.

(56) Stirling, M. J.; Sweeney, G.; MacRory, K.; Blacker, A. J.; Page, M. I. The Kinetics and Mechanism of the Organo-Iridium-Catalysed Enantioselective Reduction of Imines. *Org. Biomol. Chem.* **2016**, *14* (14), 3614–3622. https://doi.org/10.1039/C6OB00245E.

(57) Izutsu, K.; Nakamura, T.; Takizawa, K.; Takeda, A. Calorimetric Determination of Thermodynamic Parameters for the Dissociations of Acids in Dipolar Aprotic Solvents. *Bull. Chem. Soc. Jpn.* **1985**, *58* (2), 455–458. https://doi.org/10.1246/bcsj.58.455.

(58) Sampaio, R. N.; Grills, D. C.; Polyansky, D. E.; Szalda, D. J.; Fujita, E. Unexpected Roles of Triethanolamine in the Photochemical Reduction of CO 2 to Formate by Ruthenium Complexes. *J. Am. Chem. Soc.* **2020**, *142* (5), 2413–2428. https://doi.org/10.1021/jacs.9b11897.

(59) Stegbauer, L.; Zech, S.; Savasci, G.; Banerjee, T.; Podjaski, F.; Schwinghammer, K.; Ochsenfeld, C.; Lotsch, B. V. Tailor-Made Photoconductive Pyrene-Based Covalent Organic Frameworks for Visible-Light Driven Hydrogen Generation. *Adv. Energy Mater.* **2018**, *8* (24), 1–8. https://doi.org/10.1002/aenm.201703278.

(60) Chambers, M. B.; Wang, X.; Elgrishi, N.; Hendon, C. H.; Walsh, A.; Bonnefoy, J.; Canivet, J.; Quadrelli, E. A.; Farrusseng, D.; Mellot-Draznieks, C.; Fontecave, M. Photocatalytic Carbon Dioxide Reduction with Rhodium-Based Catalysts in Solution and Heterogenized within Metal-Organic Frameworks. *ChemSusChem* **2015**, *8* (4), 603–608. https://doi.org/10.1002/cssc.201403345.

(61) Lippi, R.; Coghlan, C. J.; Howard, S. C.; Easton, C. D.; Gu, Q.; Patel, J.; Sumby, C. J.; Kennedy, D. F.; Doonan, C. J. In Situ MOF-Templating of Rh Nanocatalysts under Reducing Conditions. *Aust. J. Chem.* **2020**, *73* (12), 1271. https://doi.org/10.1071/CH20193.

(62) Debye, P.; Menke, H. The Determination of the Inner Structure of Liquids by X-Ray Means. *Phys. Zeitschrift* **1930**, *31*, 797–798.

(63) Billinge, S. J. L.; Kanatzidis, M. G. Beyond Crystallography: The Study of Disorder, Nanocrystallinity and Crystallographically Challenged Materials with Pair Distribution Functions. *Chem. Commun.* **2004**, *4* (7), 749. https://doi.org/10.1039/b309577k.

(64) Petkov, V. Nanostructure by High-Energy X-Ray Diffraction. *Mater. Today* **2008**, *11* (11), 28–38. https://doi.org/10.1016/S1369-7021(08)70236-0.

(65) Takeshi, E.; Billinge, S. J. L. Total Scattering Experiments. In *Underneath the Bragg Peaks: Structural Analysis of Complex Materials*; Takeshi, E., Billinge, S. J. L., Eds.; Pergamon, 2012; pp 113–158. https://doi.org/10.1016/B978-0-08-097133-9.00004-6.

(66) Christiansen, T. L.; Cooper, S. R.; Jensen, K. M. Ø. There's No Place like Real-Space: Elucidating Size-Dependent Atomic Structure of Nanomaterials Using Pair Distribution Function Analysis. *Nanoscale Adv.* **2020**, *2* (6), 2234–2254. https://doi.org/10.1039/D0NA00120A.

(67) Bennett, T. D.; Cheetham, A. K. Amorphous Metal–Organic Frameworks. *Acc. Chem. Res.* **2014**, *47* (5), 1555–1562. https://doi.org/10.1021/ar5000314.

(68) Singh, H. P. Determination of Thermal Expansion of Germanium, Rhodium and Iridium by X-Rays. *Acta Crystallogr. Sect. A* **1968**, *24* (4), 469–471. https://doi.org/10.1107/S056773946800094X.

(69) Shimizu, K.; Oda, T.; Sakamoto, Y.; Kamiya, Y.; Yoshida, H.; Satsuma, A. Quantitative Determination of Average Rhodium Oxidation State by a Simple XANES Analysis. *Appl. Catal. B Environ.* **2012**, *111–112*, 509–514.

https://doi.org/10.1016/j.apcatb.2011.11.002.
(70) Kalecińska, E.; Jezierski, A.; Kaleciński, J.; Pruchnik, F.; Jezowska-Trzebiatowska, B. The Radiation Chemistry of Rhodium Complexes in Aqueous Alcoholic Systems. *Int. J. Radiat. Appl. Instrumentation. Part* **1990**, *36* (2), 109–112. https://doi.org/10.1016/1359-0197(90)90223-5.
(71) Kalecińska, E.; Kaleciński, J.; Pruchnik, F. P. Radiation Reduction of Binuclear Rh(II) Complexes in Aqueous-Methanol Solutions. *J. Radioanal. Nucl. Chem.* **1998**, *232* (1–2), 97–101. https://doi.org/10.1007/BF02383721.
(72) Pruchnik, F.; Jezierski, A.; Kalecińska, E. Electron Paramagnetic Resonance Study on Radiation Reduction of Dirhodium(II) [Rh2(O2CR)4] and [Rh2Cl2(O2CR)2(NN)2] Complexes. *Polyhedron* **1991**, *10* (22), 2551–2557. https://doi.org/10.1016/S0277-5387(00)81329-7.
(73) Eastland, G. W.; Symons, M. C. R. Electron Addition to Dirhodium Complexes: An Electron Spin Resonance Study. *J. Chem. Soc. Dalt. Trans.* **1984**, No. 10, 2193–2196. https://doi.org/10.1039/DT9840002193.
(74) Pruchnik, F. P. Structure and Reactivity of Rhodium(II) Complexes. *Pure Appl. Chem.* **1989**, *61* (5), 795–804. https://doi.org/10.1351/pac198961050795.
(75) Yan, Z. H.; Du, M.-H. H.; Liu, J.; Jin, S.; Wang, C.; Zhuang, G.-L. L.; Kong, X.-J. J.; Long, L.-S. S.; Zheng, L.-S. S. Photo-Generated Dinuclear {Eu(II)}2 Active Sites for Selective CO2 Reduction in a Photosensitizing Metal-Organic Framework. *Nat. Commun.* **2018**, *9* (1), 1–9. https://doi.org/10.1038/s41467-018-05659-7.
(76) Probst, B.; Rodenberg, A.; Guttentag, M.; Hamm, P.; Alberto, R. A Highly Stable Rhenium−Cobalt System for Photocatalytic H 2 Production: Unraveling the Performance-Limiting Steps. *Inorg. Chem.* **2010**, *49* (14), 6453–6460. https://doi.org/10.1021/ic100036v.
(77) Reithmeier, R.; Bruckmeier, C.; Rieger, B. Conversion of CO2 via Visible Light Promoted Homogeneous Redox Catalysis. *Catalysts* **2012**, *2* (4), 544–571. https://doi.org/10.3390/catal2040544.
(78) Yamazaki, Y.; Takeda, H.; Ishitani, O. Photocatalytic Reduction of CO2 Using Metal Complexes. *J. Photochem. Photobiol. C Photochem. Rev.* **2015**, *25* (24), 106–137. https://doi.org/10.1016/j.jphotochemrev.2015.09.001.

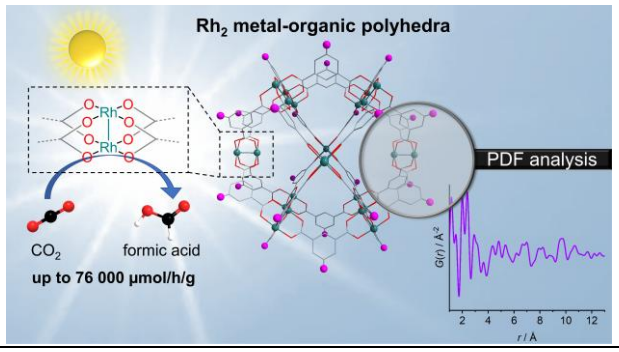
Rh2 metal-organic polyhedra
Rh
Rh
CO2
formic acid
up to 76 000 µmol/h/g
PDF analysis
G(r) / Å-2
2
4
6
8
10
12
r / Å